Nuclear Science and Techniques (2026) 37:90
https://doi.org/10.1007/s41365-026-01917-2

Coupling simulation of hydrodynamic tunneling effect induced by beam impact in high-power accelerators

Wei Zhang[1] · Chao-Fan An[1] · Yong Wang[1] · Jian Li[1] · Yuan Chen[1] · Zhi-Xin Tan[2,3] · Tao Yang[4] · Yuan-Cun Nie[1]

Received: 15 October 2024 / Revised: 25 November 2024 / Accepted: 28 November 2024 / Published online: 7 March 2026

Abstract
Under certain accident conditions in particle accelerators, high-power beam irradiation may damage vacuum pipes, magnets, and other key equipment. Therefore, machine protection for high-power accelerators is critical to ensure safe operation. It is important to study radiation damage to materials to support the design and operation of machine protection systems. In the shock-wave regime, a pronounced hydrodynamic tunneling effect occurs within materials. The traditional one-way coupling simulation method results in substantial errors in this regime. Therefore, a bidirectional iterative coupling simulation method was developed. This method enables the bidirectional coupling of the Monte Carlo code FLUKA and the thermodynamic program Ansys-Autodyn. Density changes are monitored during the simulations, and the updated density is promptly fed back to FLUKA. The program remodels the target with the new density distribution to calculate the new energy deposition distribution, which is then returned to Autodyn for subsequent simulations. This iterative process continues until the entire beam has completed the energy deposition process. Compared to existing methods, this automated method significantly improves the efficiency of the coupled simulations and reduces the possibility of human error. The HRMT-12 beam irradiation experiment at CERN was used for a benchmark study, and simulations were conducted and compared using different equations of state. The results demonstrate the efficiency and accuracy of this simulation method. Compared to complex and costly beam irradiation experiments, this approach is expected to provide fast and cost-effective scientific guidance for the machine protection of high-power accelerators. Considering the severe consequences of the hydrodynamic tunneling effect, machine protection components such as beam collimators, absorbers, and dump blocks should adopt low-density materials to reduce the energy deposition density. Beam dilution may be required in beam dumping systems to avoid target damage. This method can be applied to the redundancy design of such beam dumping systems.

Keywords High-power accelerators · Machine protection · Irradiation damage · Monte Carlo simulation · Thermodynamic response

This work was supported by the National Natural Science Foundation of China (No. 12275196).

✉ Yuan-Cun Nie
nieyuancun@whu.edu.cn

1 The Institute for Advanced Studies, Wuhan University, Wuhan 430072, China

2 Institute of High Energy Physics, Chinese Academy of Sciences, Beijing 100049, China

3 Spallation Neutron Source Science Center, Dongguan 523803, China

4 Institute of Plasma Physics, Hefei Institutes of Physical Science, Chinese Academy of Sciences, Hefei 230031, China

1 Introduction

High-energy particle accelerators, as fundamental tools of modern physics research, are widely used in various fields, including multidisciplinary exploration, materials science, medicine, and energy research. However, when accelerators experience malfunctions or operational errors, radiation damage to the accelerator components caused by high-power particle beams can severely impact the entire facility [1]. Beam losses may not only lead to material activation but also result in damage to key equipment [2–5]. Particularly under abnormal conditions, if materials fail to effectively withstand the radiation load, it may lead to the destruction of vacuum pipes, magnets, and other key equipment.

Therefore, a complete machine protection system is essential for ensuring safe and stable operation of high-power accelerators [6–8].

Material damage caused by beam irradiation is an important research topic within the framework of machine protection [9]. In particular, under beam accident conditions, high-power beams may damage critical accelerator components, further affecting the operation of the entire facility. Over the past few decades, accelerators worldwide have recorded incidents involving various degrees of radiation damage to materials. For instance, the Super Proton Synchrotron (SPS) at CERN once accidentally deflected 288 proton bunches at 450 GeV into the transfer line while injecting the beam into the Large Hadron Collider (LHC), damaging part of the beamline and magnets [10]. The RHIC accelerator at Brookhaven National Laboratory has also experienced incidents in which beam losses damaged key experimental detectors [11].

The radiation damage caused by high-power beams often results in extreme changes in the physical states of materials, such as rapid temperature increases and melting [12, 13]. Researchers have classified the mechanical responses of materials into three regions based on the time of the beam energy deposition and the power density of the energy deposition: the elastic, plastic, and shock-wave regimes [14]. Generally, when the energy deposition density is less than 100 J/cm^3, the material's response remains within the elastic dynamic range [15, 16]. This means that the vibrations and stress waves induced by energy deposition do not exceed the material's elastic limit, allowing the mechanical structure of the material to return to its initial state after beam irradiation [17, 18]. When the energy deposition density is between 10 J/cm^3 and 100 J/cm^3, localized stress waves are expected to exceed the material's elastic limit, leading to permanent plastic deformation [19]. Finally, if the energy deposition density exceeds 10 J/cm^3, the strength of the stress waves will be sufficient to change the density and cause mechanical damage, such as fragmentation or explosion, to the material. For metallic materials, phase transitions typically occur, resulting in the formation of liquids, gases, or even plasmas. This is why this region is referred to as the shock-wave regime [20, 21]. In this region, the target is generally continuously irradiated by a high-energy bunch train, experiencing rapid increases in temperature and pressure, often accompanied by phase transitions such as melting, vaporization, and even plasmonization [22]. Near the central axis where the irradiation is the most severe and the energy deposition is the most concentrated, material particles are subjected to high-temperature and high-pressure fields, causing transverse displacement perpendicular to the axis. Owing to the transverse impact of the pressure waves, the material density gradually decreases around the axis where the initial energy deposition is concentrated [23, 24]. Consequently, subsequent bunches and their secondary particles can more easily pass through these low-density regions, creating new energy deposition spatial distributions deeper within the material. This phenomenon is known as the hydrodynamic tunneling effect [25, 26].

Regarding experimental research on the hydrodynamic tunneling effect, as early as the 1970 s, the SLAC laboratory in the USA conducted an experiment in which an 18 GeV, 500 kW electron beam irradiated a copper block. The beam spot had a diameter of approximately 2 mm, and the irradiation lasted for 1.3 s, resulting in an observed melting path of nearly 30 cm along the copper block [27]. To date, the most active international platform for research on high-power beam radiation damage is the high radiation to materials (HiRadMat) facility at CERN [28–30]. The primary goal of HiRadMat is to conduct beam--target experiments using high-energy proton and ion beams generated by the SPS. These experiments mainly aim to develop and test new materials for the LHC, which are used in beam collimators, beam absorbers, beam windows, etc. At HiRadMat, the beam spot size can be adjusted within the range of $0.5 - 2.0$ mm. Combined with variable beam intensities, this allows for the study of material responses under different energy deposition densities.

Because beam irradiation experiments are generally quite expensive, numerical simulations are preferred in most cases to study the interactions between beams and materials, thereby supporting the design of relevant machine protection components [31, 32]. Currently, numerical simulation methods in the elastic and plastic regimes are relatively well developed [33, 34]. In the elastic interaction region, Monte Carlo simulation programs such as FLUKA [35], MARS [36], and GEANT4 [37] can be used to calculate the energy deposition behavior of a single normalized particle within the material. As the number of particles increases, the energy deposition can be scaled up linearly, and the resulting material temperature increase can be estimated in a straightforward manner [38]. In the plastic regime, Monte Carlo simulations can be coupled with finite element analysis software such as Ansys [39] to calculate the mechanical response of the material. However, in the shock-wave regime, it is essential to couple Monte Carlo simulations with thermodynamic software, such as Ansys-Autodyn or Ansys LS-DYNA, to study the material's response and final physical state [40–42]. Historically, such simulations have often been linked through a one-way coupling, as illustrated in Fig. 1. Initially, a Monte Carlo simulation program such as FLUKA is used to calculate the spatial distribution of the energy deposition of high-energy particles within the material. This energy deposition distribution is then imported into thermodynamic software as a one-time energy input for thermomechanical response analysis [43]. This approach includes a static approximation, assuming that the material's

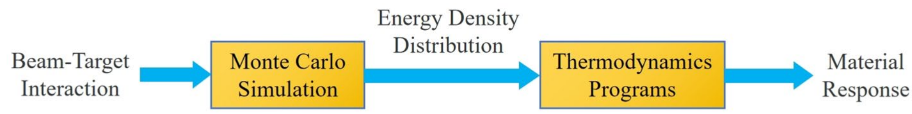

Fig. 1 (Color online) Schematic diagram of the one-way coupling simulation method

physical density does not significantly change during beam irradiation, or that the density changes are not sufficient to significantly alter the subsequent spatial distribution of energy deposition induced by the following particles. However, as previously mentioned, in the shock-wave regime, the hydrodynamic tunneling effect will probably occur as the target is continuously irradiated by a high-power bunch train. A static approximation can lead to considerable calculation errors. Therefore, a bidirectional iterative coupling simulation, as illustrated in Fig. 2, is necessary. This involves monitoring the changes in material density during the beam-target interaction and sending this updated density information back to the Monte Carlo code in a timely manner. The Monte Carlo program can then re-model the target by using the new density distribution to calculate a new energy deposition distribution. This updated energy deposition distribution is subsequently transferred back to the thermodynamic program for further simulations. This iterative process continues until all bunches in the beam have completed the energy deposition process.

To date, there have been few reports on bidirectional iterative coupling simulations. Recently, Tahir et al. reviewed their relevant works [44], studying the hydrodynamic tunneling effect that may be induced by beam-material interactions in high-power accelerators such as SPS, LHC, and FCC (planned) at CERN through iterative coupling simulations between FLUKA and BIG2. These studies have shown that, compared to previous one-way coupling simulations using a static approximation, the irradiation damage depth of high-power beams in copper and graphite materials increases by an order of magnitude when the hydrodynamic tunneling effect is properly considered. In general, methods for simulating the hydrodynamic tunneling effect are not well developed. First, BIG2 is a two-dimensional dynamic program that cannot effectively simulate non-axisymmetric beam--target interactions. Second, data processing and model reconstruction were essentially performed manually in previous studies, leading to low computational efficiency. Finally, it is important to mutually verify and supplement such complex simulations using different programs, particularly when experiments are difficult to perform.

This paper reports the recent development of a bidirectional iterative coupling simulation method to study the hydrodynamic tunneling effect. As a new complement, FLUKA and Ansys-Autodyn were automatically coupled using Python scripts. In this way, the simulation accuracy, efficiency, and reliability can be improved. Using the HRMT-12 beam irradiation experiment at CERN as an example, simulations were performed with the corresponding beam parameters to validate the accuracy of the bidirectional iterative coupling simulation method. The results obtained using different equations of state (EOS) were also analyzed to better understand the hydrodynamic tunneling effect.

In Sect. 2, the beam and model parameters used in the HRMT-12 experiment and simulations are described. The automation of the bidirectional iterative coupling is introduced in Sect. 3. In Sect. 4, we present the results obtained from the automated iterative coupling simulations with different equations of state and compare the simulation and experimental results, primarily focusing on the penetration depth of the beam into the target. The conclusions drawn from this study are summarized in Sect. 5.

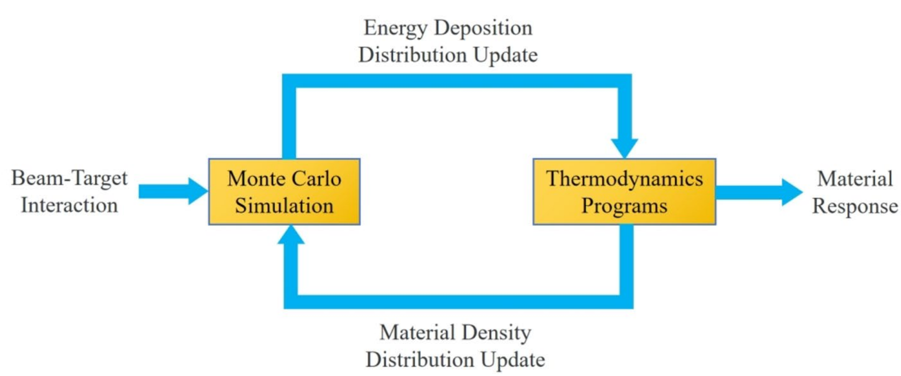

Fig. 2 (Color online) Schematic diagram of the bidirectional iterative coupling simulation method

2 HRMT-12 experiment and modeling parameters

2.1 HRMT-12 experiment at CERN

In 2012, CERN conducted a series of high-energy beam irradiation experiments on copper targets at the HiRadMat facility using the SPS beam [29, 30, 45]. Three sets of copper targets were used, each consisting of 15 cylindrical copper blocks with a spacing of 1 cm, a radius of 4 cm, a length of 10 cm, and a material density of 8.93 g/cm^3. One of the three sets of targets is illustrated in Fig. 3.

The first two copper target sets were irradiated with 144 and 108 proton bunches, respectively, where the RMS beam size was maintained at $\sigma = 0.2$ mm following a two-dimensional Gaussian distribution, whereas the third target set was irradiated at a beam size of $\sigma = 2$ mm with 144 bunches. The beams were directed perpendicularly to the end face of the copper targets, aiming at the central axis for continuous irradiation. The detailed beam parameters used in the experiment are listed in Table 1.

During the irradiation experiment, the three sets of copper targets were covered with a top plate. After the experiment, the regions that exhibited the hydrodynamic tunneling effect were first evaluated by observing traces of copper melting or evaporation on the top cover, and then accurately analyzed by cutting the copper target and performing electron microscopy observations [30]. An image of the top plate after the irradiation experiment can be found in the published paper [45].

2.2 Simulation modeling

2.2.1 Beam parameters used in the simulations

To verify the accuracy and reliability of the simulation program, numerical simulations were performed and compared with the three sets of experimental results from HRMT-12. In the simulations, the detailed beam parameters and beam time structures were the same as those listed in Table 1.

2.2.2 Copper target parameters and zoning in FLUKA

As in the previous simulations using FLUKA and BIG2, small gaps between adjacent copper cylinders were neglected [45, 46]. In FLUKA, a cylindrical copper target with a radius of 4 cm, a length of 150 cm, and a density of 8.93 g/cm^3 was established. Based on the energy deposition distribution of the first bunch in the copper target, the transverse x–y plane was divided into regions with energy deposition and regions with almost no energy deposition. The longitudinal region along the z direction was divided based on the HiRadMat experimental results. The zoning results are shown in Fig. 4.

A model with 2500 regions was chosen as a compromise between resolution and FLUKA runtime. This entailed a

Fig. 3 (Color online) Arrangement diagram of a target set consisting of 15 copper blocks used in the HRMT-12 experiment, where the proton beam irradiated the targets from left to right

Table 1 Detailed parameters and time structure of the proton beams used in the HRMT-12 experiment

Particle energy (GeV)	Bunch intensity (protons per bunch)	Bunch length (ns)	Bunch spacing (ns)	RMS beam emittance (πmm · mrad)	Number of bunches per package	Package spacing (ns)	Number of bunches
440	1.5×10^{11}	0.5	50	3.5	36	250	144/108

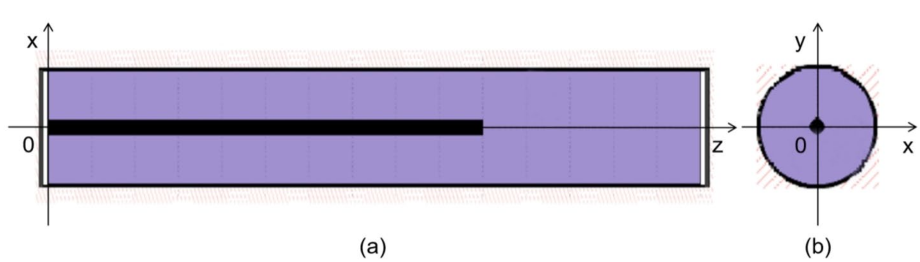

Fig. 4 (Color online) Zoning of the FLUKA target: **a** the x–z sectional view at $y = 0$; **b** the x–y sectional view at $z = 0$

running time of up to two days. In the region with significant energy deposition, detailed zoning was performed from $r = 0$ to 0.5 cm and $z = 0$ to 100 cm. In the simulations, radial zoning was conducted from the central axis $r = 0$ cm to $r = 0.5$ cm in increments of $\Delta r = 0.01$ cm, half of the beam size of $\sigma = 0.2$ mm. Longitudinal zoning was performed from the beam entry surface at $z = 0$ cm to $z = 100$ cm in increments of $\Delta z = 2$ cm. The zoning results are shown in Fig. 5.

The spatial dose distribution was scored using regular binning. The angular coordinates from 0 to 2π spanned one bin, taking advantage of the circular symmetry condition. To ensure a sufficiently high spatial resolution close to the target axis, where the largest density gradients occurred, a radial binning width of 0.05 mm was chosen, corresponding to one-fourth of the beam size of $\sigma = 0.2$ mm, and an axial binning size of 2 mm was adopted.

2.2.3 Material response in Autodyn

Autodyn is used for explicit analysis of the nonlinear dynamics of materials, where the dynamics of continuous media are described by a set of differential equations derived from the principles of conservation of energy, mass, and momentum. The EOS connects the density, temperature, and pressure of a material across different physical phases [47]. In Autodyn, the time structure of the beam was considered using a calculation time step of 0.5 ns. The grid was divided longitudinally from 0 to 1500 mm into 750 cells, each measuring 2 mm. The radial grid was divided from 0 to 40 mm into 800 cells each measuring 0.05 mm. A total of 600,000 cells were included, and the calculation required approximately half a day. In Autodyn, the commonly used shock and Tillotson equations of state for solid copper targets can be selected and employed [48], along with the Johnson-Cook strength and failure model suitable for solid copper targets [49, 50].

The shock equation of state is used to describe the behavior of materials under high pressures, particularly during shock-wave propagation. Its basic form is:

$$P = \rho \cdot \epsilon \cdot \left(1 + \Gamma \cdot \frac{\epsilon}{P_0}\right), \tag{1}$$

where P is the pressure, ρ is the density, ϵ is the specific internal energy, P_0 is the reference pressure (usually zero or atmospheric pressure), and Γ is the Grüneisen parameter, which describes the relationship between energy and volume changes.

The Tillotson equation of state is used to describe the thermodynamic properties of solids, liquids, and gases under extreme conditions, particularly in shock-wave propagation and explosion simulations. This equation is expressed as a piecewise function to describe the relationship between pressure, volume, and temperature in different states of matter. Its basic form is:

$$P = \frac{A}{\rho_0}\left[1 - \frac{V}{V_0}\right] + B\left(1 - \frac{V_0}{V}\right), \tag{2}$$

where P is the pressure, ρ_0 is the initial density, V is the volume, V_0 is the reference volume (usually the volume at zero pressure), and A and B are constants that depend on the material and its thermodynamic state.

The threshold for the change in material density in the energy deposition regions was set to approximately 10% in Autodyn to achieve a sufficient simulation accuracy of approximately 10%. Figure 6 shows the changes and distribution of the physical states (density, temperature, and pressure) of the target during beam irradiation, as simulated by Autodyn. After continuous irradiation with 12 bunches, a low-density region gradually formed within the target. The right plot shows the observed density, temperature, and pressure over time at the red dot in the left plot.

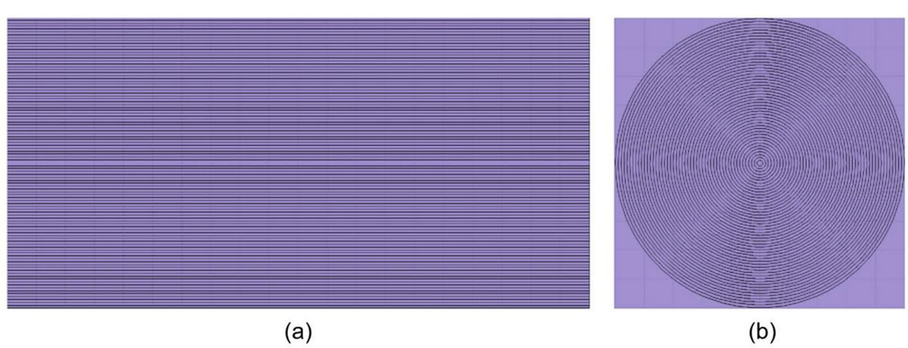

Fig. 5 (Color online) Local display of the zoning in FLUKA target for $r = 0$ to 0.5 cm, and $z = 0$ to 100 cm: **a** the frontal view with the longitudinal length divided into 2 cm sections; **b** the left view with radial zoning starting from the central axis $r = 0$ cm in increments of $\Delta r = 0.01$ cm

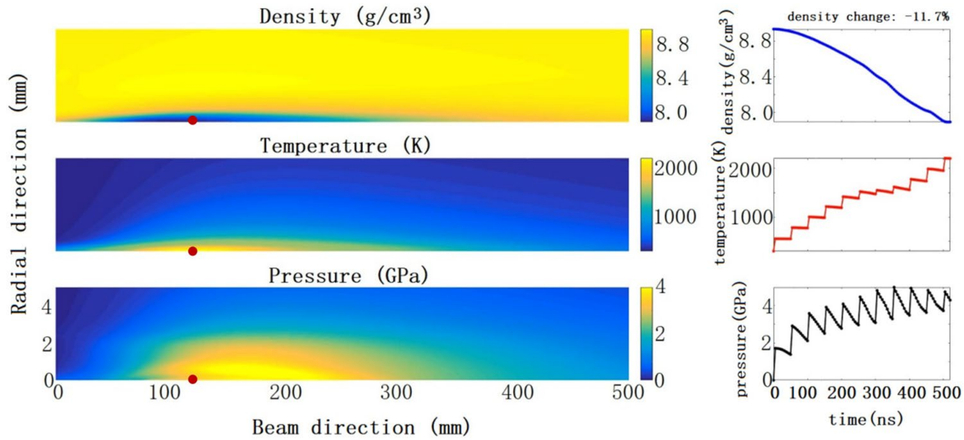

Fig. 6 (Color online) Autodyn parameter output for material response after irradiation with 12 proton bunches

3 Automation of the bidirectional iterative coupling

3.1 Introduction to automated coupling simulation

In the bidirectional iterative coupling simulation between the energy deposition code FLUKA and the hydrodynamic code Autodyn, both programs must be executed in a loop to recalculate the energy deposition and target density at each iteration. This results in a time-consuming simulation process, with a single case study typically requiring several months to complete. Currently, the overall runtime is primarily determined by the Monte Carlo energy deposition code. In fact, the manual intervention required in each simulation iteration becomes a critical bottleneck for efficient studies of the hydrodynamic tunnel effect. Therefore, we developed a coupling script written in Python. The script reads the material density from Autodyn output files, interpolates it, assigns it to the corresponding FLUKA regions, and automatically generates new FLUKA input files. Whereas these steps were previously carried out semi-automatically in the established workflow [47], the new method improves time efficiency by minimizing the required manual operations and reducing the likelihood of human error. Currently, the time required to study a case has been reduced to approximately one month.

3.2 Script structure

The script described in this paper covers the workflow from reading the Autodyn output files to generating new FLUKA input files with updated material densities. The script only requires input files containing the coordinates and corresponding densities from Autodyn simulations; it automatically reads these files and generates new FLUKA input files. The script structure is as follows:

1. Data Processing: The script first reads the density data from the Autodyn output files and processes them to remove unnecessary header information. The processed data are then saved to a new text file.
2. Preprocessing: The script reads the data obtained from the last step and further processes and filters them to remove rows where the density value is less than or equal to zero.
3. Interpolation: The filtered data are sorted and interpolated using a two-dimensional interpolation method.
4. Generating FLUKA Input Files: The interpolated data are used to generate FLUKA input files. The input files include sections defining the beam characteristics, beam position, geometry, materials, and regions used in the simulation.

As shown in Fig. 7, during a complete simulation cycle, the newly generated input files are subsequently run using FLUKA, and the resulting specific energy deposition is imported into Autodyn to simulate the hydrodynamic effects of subsequent bunches on the target material. These iterations are repeated until all bunches in the beam have impacted the target.

4 Simulation results

4.1 Temperature

Figure 8 displays two-dimensional temperature maps obtained in Autodyn using different equations of state. Comparing the four plots in Fig. 8a–d shows that regardless of whether the shock or Tillotson EOS is used, around the axis of the copper target, the temperature at the initially irradiated positions gradually increases with the number of delivered bunches. As the number of bunches increases, the depth of the irradiation effect increases. Compared to the Tillotson EOS, the shock EOS is more commonly used to describe the behavior of materials under shock-wave conditions without considering phase transitions. Consequently, energy is

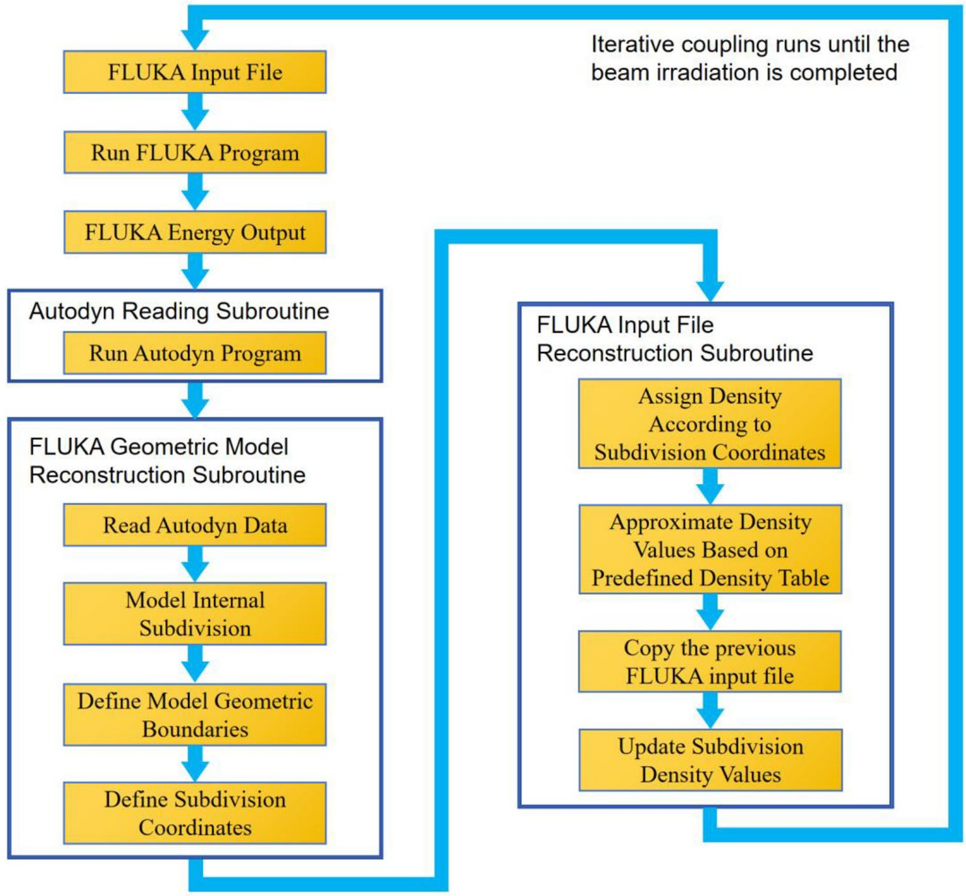

Fig. 7 (Color online) Flowchart of the automated implementation of bidirectional iterative coupling simulation between FLUKA and Autodyn

mainly concentrated on compression and temperature rise, rather than on complex phase transitions and ionization processes. Therefore, the deposited energy is more directly converted into thermal energy, leading to a faster rate of temperature increase. In contrast, the Tillotson EOS considers more complex behaviors of materials during compression and expansion, including partial ionization and phase changes. As a result, the energy conversion and distribution are more complex, and the rate of temperature increase may be slower because a portion of the energy is used for the phase transition and ionization processes. Copper exhibits significant ionization at approximately 10,000 K, which is why a larger temperature range exceeding 10,000 K is observed when the shock EOS is applied in Autodyn simulation, where phase changes and ionizations are not considered. Comparing the plots shown in Fig. 8c–f indicates that with the increase in the beam size from 0.2 to 2 mm, the maximum temperatures simulated by using the shock and Tillotson EOS are both around 4,000 K, with little difference between them. In this case, with lower energy deposition density compared to that observed for the beam size of 0.2 mm, the effects of phase transitions and ionizations are not significant.

In Fig. 8, for each image, a black line has been inserted to represent the melting point of copper. The areas inside the line correspond to temperatures above the melting point, whereas those outside the line correspond to temperatures below the melting point. When the temperature at a certain point reaches the melting point of copper, the copper needs to continue absorbing heat to melt, owing to the latent heat of melting. Therefore, a melting region in between the solid and melted states exists. For the shock EOS, with a 2-mm beam size and 144 bunches, the melting region is between 49 and 52 cm; for a 0.2-mm beam size and 108 bunches, it is between 73 and 75 cm; and for a 0.2-mm beam size and 144 bunches, it is between 80 and 83 cm. For the Tillotson EOS, with a 2-mm beam size and 144 bunches, the melting region is between 55 and 58 cm; for a 0.2-mm beam size and 108 bunches, it is between 80 and 84 cm; and for a 0.2-mm beam size and 144 bunches, it is between 90 and 93 cm.

4.2 Pressure

Figure 9 shows the two-dimensional pressure distributions obtained using different equations of state in Autodyn simulations. Comparing the plots in Fig. 9a–d shows that regardless of whether the shock or Tillotson EOS is used, around the target axis, the pressure at the initially irradiated positions gradually rises as the number of irradiated

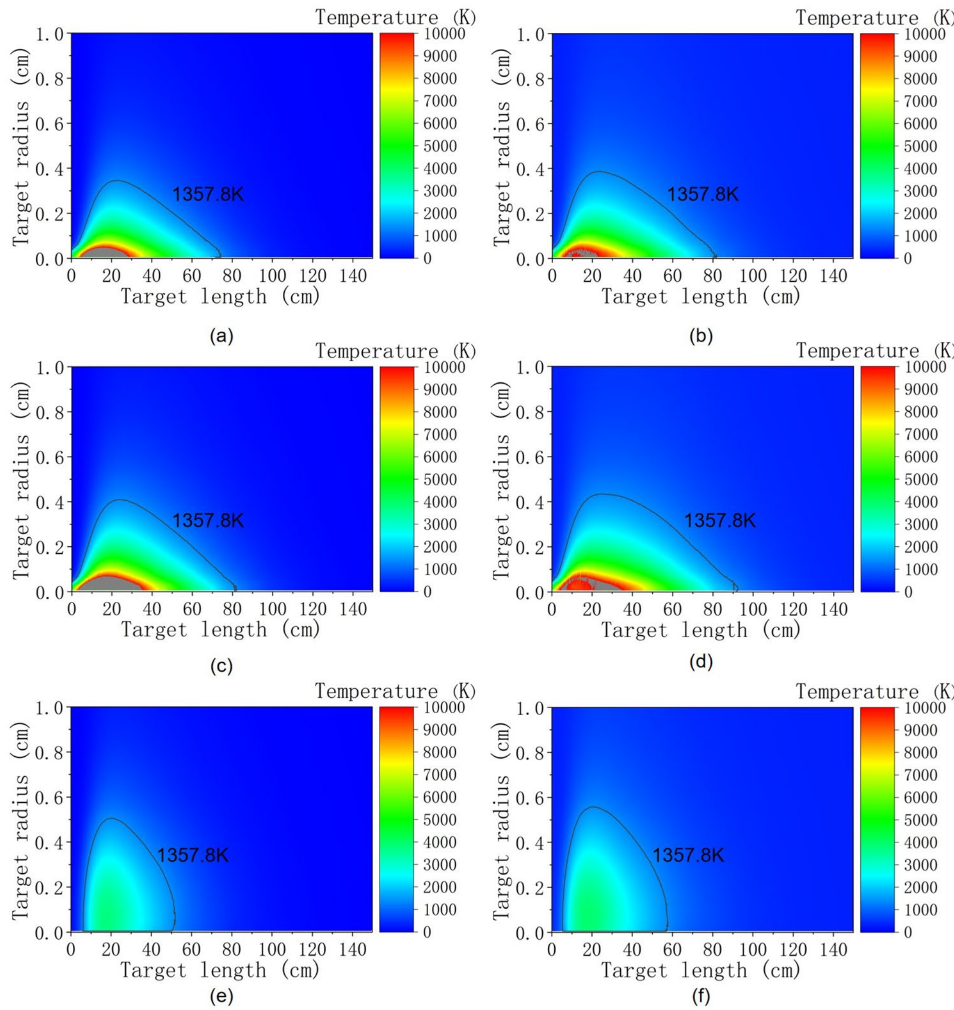

Fig. 8 (Color online) Two-dimensional temperature distributions in the $r-z$ plane calculated using Autodyn using the shock and Tillotson equations of state: **a** Using the shock EOS, with a beam size of 0.2 mm, after 108 bunches; **b** using the Tillotson EOS, with a beam size of 0.2 mm, after 108 bunches; **c** using the shock EOS, with a beam size of 0.2 mm, after 144 bunches; **d** using the Tillotson EOS, with a beam size of 0.2 mm, after 144 bunches; **e** using the shock EOS, with a beam size of 2 mm, after 144 bunches; **f** using the Tillotson EOS, with a beam size of 2 mm, after 144 bunches

bunches increases. Additionally, the high-pressure area penetrates deeper into the target as more bunches irradiate it. This indicates that although different equations of state have varying effects on the specific pressure values when describing material behaviors under high pressure, their influence on the pressure accumulation trend is similar. Both the shock and Tillotson equations of state are suitable for high-pressure environments, leading to similar pressure distribution patterns under these high-energy-density conditions. The application of different equations of state has a minor effect on the peak pressure, reflecting subtle differences in the energy transfer patterns within the irradiation region. When comparing Fig. 9c–f, it is evident that as the beam size increases from 0.2 mm to 2 mm, the pressure distribution characteristics significantly change. Although the lateral extent of the compressed area expands with increasing beam size, the maximum pressure decreases. This is consistent with the temperature distributions shown in Fig. 8, where the larger beam size leads to lower energy density and temperature, resulting in lower generated pressures.

4.3 Density

Figure 10 plots two-dimensional density distributions obtained using different equations of state in Autodyn. From Fig. 10a–d, regardless of which EOS is used, around the target axis, the density at the initially irradiated positions gradually decreases as the number of irradiated bunches increases. The low-density area penetrates deeper into the target as more bunches irradiate it. After 108 bunches, differences between the shock and Tillotson equations of state appear, in which the Tillotson EOS shows a more significant reduction in density. After 144 bunches, the density reduction in the shock EOS case is apparently smaller, whereas the minimum density in the Tillotson EOS case drops to nearly zero, that is, a hollow cavity is formed in the target. The shock equation handles complex processes such as phase transitions and ionizations in a relatively simple manner, and most of the deposited energy is concentrated in the temperature rise and compression. In the case of the shock EOS, the rapid temperature increase under beam impact leads to strong compression, allowing the material's microstructure

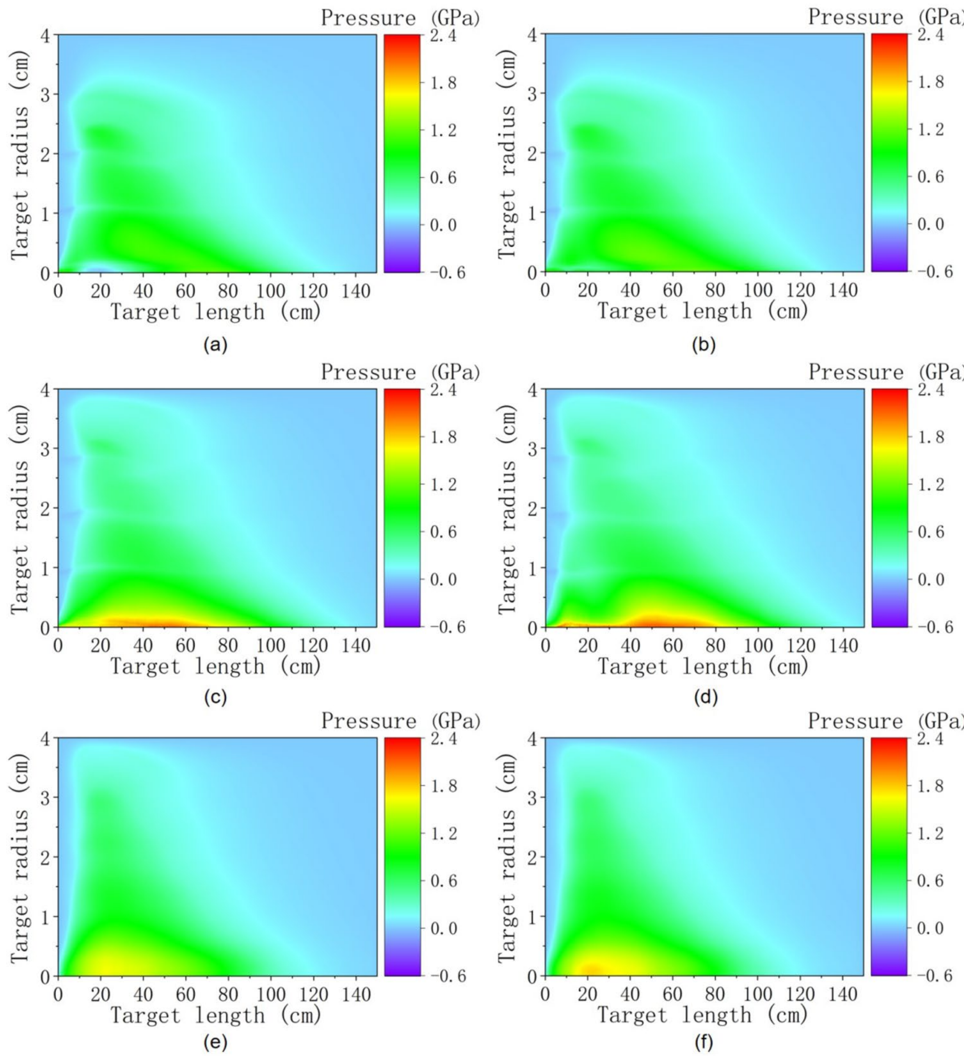

Fig. 9 (Color online) Two-dimensional pressure distributions in the $r - z$ plane calculated by Autodyn using the shock and Tillotson equations of state: **a** Using the shock EOS, with a beam size of 0.2 mm, after 108 bunches; **b** using the Tillotson EOS, with a beam size of 0.2 mm, after 108 bunches; **c** using the shock EOS, with a beam size of 0.2 mm, after 144 bunches; **d** using the Tillotson EOS, with a beam size of 0.2 mm, after 144 bunches; **e** using the shock EOS, with a beam size of 2 mm, after 144 bunches; **f** using the Tillotson EOS, with a beam size of 2 mm, after 144 bunches

to quickly adapt to these temperature changes. Consequently, even though the temperature increases significantly in the target materials, the internal structure remains stable, resulting in higher density retention. In contrast, the Tillotson EOS considers the complex behaviors of target materials under high temperatures and pressures, including phase transitions and ionization. When exposed to a high-power beam, the Tillotson equation allows for more pronounced phase changes and partial ionization. As the temperature increases, the atomic and molecular motion intensifies, causing more atoms to become unbound and enter the liquid, gaseous, or plasma states, leading to a significant reduction in material density. From Fig. 10c–f, it can be observed that for both the shock and Tillotson equations of state, the level of density reduction decreases as the beam size increases from 0.2 to 2 mm. In the case of a 2-mm beam size, the temperatures predicted by both equations are similar, resulting in relatively minor differences in the density distributions. In general, the density reduction is greater when the Tillotson EOS is used; we believe that this result is closer to the actual situation.

In Fig. 10, for each image, the shaded areas indicate regions where the density exceeds 8.93 g/cm^3 due to compression. Because the entire radial range that we calculated is from 0 to 4 cm, the parts with densities greater than 8.93 g/cm^3 beyond the vertical coordinate range are not shown.

4.4 Results comparison

Figure 11 compares the development of the energy deposition distributions as more bunches successively irradiate the copper target. As shown, significant errors are introduced when the static approximation or unidirectional coupling is applied, as energy deposition changes considerably with density variations. From Fig. 11a, it is clear that as the number of bunches increases, the energy deposition peak decreases, and the energy deposition range

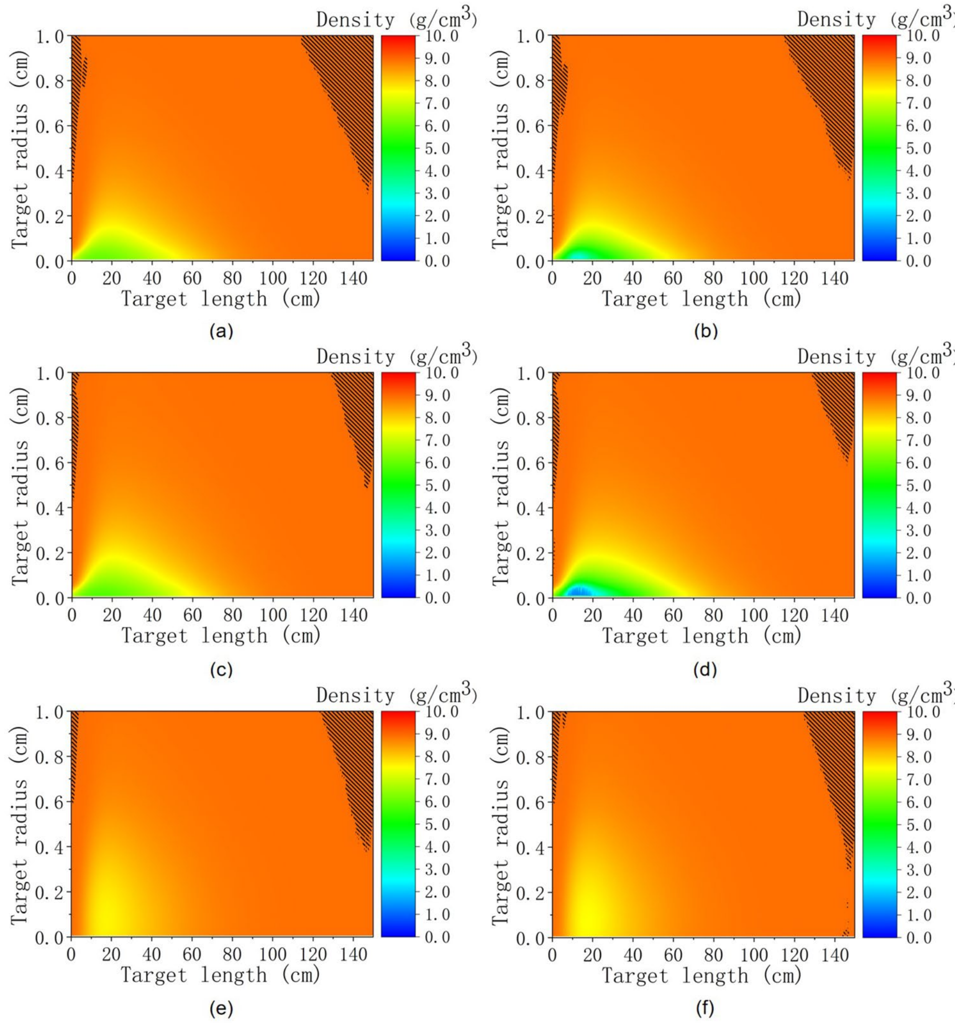

Fig. 10 (Color online) Two-dimensional density distributions in the $r-z$ plane calculated by Autodyn using the shock and Tillotson equations of state: **a** Using the shock EOS, with a beam size of 0.2 mm, after 108 bunches; **b** using the Tillotson EOS, with a beam size of 0.2 mm, after 108 bunches; **c** using the shock EOS, with a beam size of 0.2 mm, after 144 bunches; **d** using the Tillotson EOS, with a beam size of 0.2 mm, after 144 bunches; **e** using the shock EOS, with a beam size of 2 mm, after 144 bunches; **f** using the Tillotson EOS, with a beam size of 2 mm, after 144 bunches

expands, with a noticeable double-peak behavior at 7.2 μ μs. Comparing Fig. 11a and c indicates that as the beam size increases, the maximum energy deposition decreases, and the hydrodynamic tunneling effect becomes weaker. Comparing Fig. 11a and c with Fig. 11b and d, the attenuation of the energy deposition can be observed at a larger radius.

The target damage caused by beam irradiation can be assessed by evaluating the melting depth. Table 2 lists a comparison of the molten depths in Targets 1 (beam size 0.2 mm, 144 bunches), 2 (beam size 0.2 mm, 108 bunches), and 3 (beam size 2 mm, 144 bunches) between the simulations and measurements [29, 30]. As shown, when the shock EOS is used, the melting depth is slightly smaller than the measured value. In the case of the Tillotson EOS, the melting depth is slightly larger; however, the overall simulation results agree well with the measurement values, with an error within 10%.

5 Conclusions and outlook

Uncontrolled beam losses can potentially damage accelerator components during the operation of high-energy, high-power particle accelerators. Studying the interaction between high-power beams and accelerator component materials, and establishing appropriate machine protection devices in regions where energy deposition may be concentrated, are crucial to reduce the risk of damage to accelerator components.

During the high-power beam irradiation of a target, energy deposition may lead to changes in the density, temperature, and pressure of the target materials. Simulation of the hydrodynamic tunneling effect requires bidirectional iterative coupling between Monte Carlo code (such as FLUKA) and thermodynamic software (such as Autodyn), which was not previously well developed. An

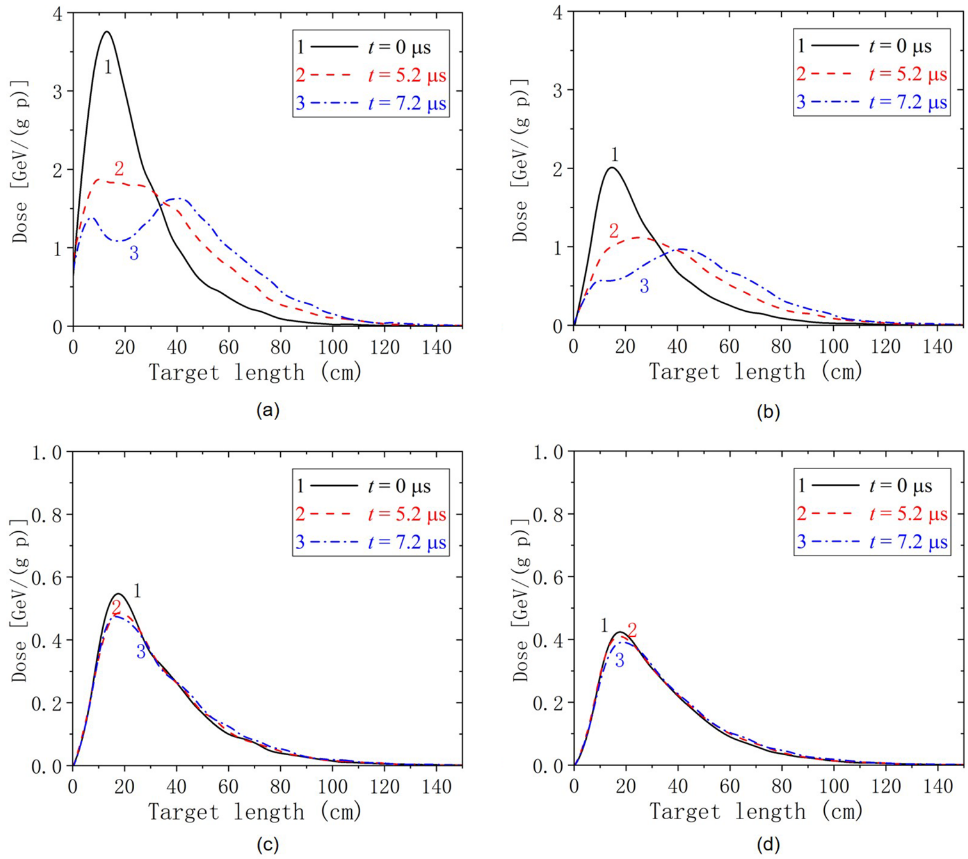

Fig. 11 (Color online) One-dimensional dose distributions calculated using FLUKA using the Tillotson EOS at different times: **a** Beam size 0.2 mm, around $r = 0$; **b** beam size 0.2 mm, around $r = 0.5$ mm; **c** beam size 2 mm, around $r = 0$; **d** beam size 2 mm, around $r = 2$ mm

Table 2 Comparison of melting depths between simulations and measurements

Target number	Beam energy (MJ)/beam power (TW)	Measurement (cm)	Shock EOS (cm)	Tillotson EOS (cm)
1 ($\sigma = 0.2$ mm, 144 bunches)	1.5/0.192	85	80–83	90–93
2 ($\sigma = 0.2$ mm, 108 bunches)	1.1/0.141	79.5	73–75	80–84
3 ($\sigma = 2$ mm, 144 bunches)	1.5/0.192	58	49–52	55–58

automated iterative coupling simulation method based on Python was developed to improve the coupling efficiency between the two software programs. This method can automatically read material densities from Autodyn output files, assign them to predefined FLUKA regions, and generate new FLUKA input files using the updated density data. The new automated iterative coupling method was benchmarked against beam experiments conducted at the HiRadMat facility of CERN, using both the shock and Tillotson equations of state for comparative simulations. A comparison between the simulation results using the two different equations of state and the measurement results showed that the Tillotson EOS provided better consistency in the melting depth of the target after beam irradiation. This is because the Tillotson EOS considers the state changes of materials more comprehensively, including critical phase transitions under high-power beam impact. Additionally, the Tillotson EOS can capture the complex dynamic processes of rapid dynamic loading and energy transfer that target materials undergo during hydrodynamic tunneling. Although the shock EOS is relatively simple and easy to use, the Tillotson EOS, with its more accurate physical descriptions and experimental validations, is better suited for simulating hydrodynamic tunneling effects. The method reported here is more efficient and practically applicable compared to methods given by previous studies, as Autodyn is able to deal with three-dimensional or non-axisymmetric targets. This study shows that the consequences of the hydrodynamic tunneling effect are severe, because the target could be destroyed if the energy deposition density is sufficiently high. For the design of machine protection components such as beam collimators, absorbers, and dump blocks, materials with lower densities (e.g., graphite or even water) should be applied to reduce the energy deposition density. In addition, beam dilution measures might be required in the beam dumping system; for instance, horizontal and vertical dilution kickers are used to sweep the beam density on the front face of the LHC beam dump block. A similar beam dilution method is considered for the FCC as well. The simulation method can be applied to the redundancy design of such beam dumping systems. Further numerical simulations and comparative analyses of additional cases will be conducted in the future using the developed method, thereby providing important references for the design of machine protection systems for high-power accelerators.

Acknowledgements The authors thank Dr. R. Schmidt, Dr. D. Wollmann, Dr. C. Wiesner, and Dr. F. Carra from CERN, Switzerland and Dr. N. Tahir from GSI, Germany, for their long-term and fruitful discussions on the hydrodynamic tunneling effect and machine protection of high-power particle accelerators.

Author contributions All authors contributed to the study conception and design. Material preparation and data collection and analysis were performed by Wei Zhang and Yuan Cun Nie. The first draft of the manuscript was written by Wei Zhang, and Yuan Cun Nie reviewed and edited the manuscript. All authors commented on previous versions of the manuscript. All authors read and approved the final manuscript.

Data availability The data that support the findings of this study are openly available in Science Data Bank at https://cstr.cn/31253.11.sciencedb.j00186.00908 and https://www.doi.org/10.57760/sciencedb.j00186.00908.

Declarations

Conflict of interest The authors declare that they have no conflict of interest.

References

1. R. Schmidt, R. Assmann, E. Carlier et al., Protection of the CERN large hadron collider. New J. Phys. **8**, 290 (2006). https://doi.org/10.1088/1367-2630/8/11/290
2. Y. Nie, R. Schmidt, V. Chetvertkova et al., Numerical simulations of energy deposition caused by 50 MeV–50 TeV proton beams in copper and graphite targets. Phys. Rev. Accel. Beams **20**, 081001 (2017). https://doi.org/10.1103/PhysRevAccelBeams.20.081001
3. R.S. Augusto, A. Trudel, J. Mildenberger et al., Impact study of beam losses in TRIUMF's BL4N proton cave and ARIEL tunnel. Nucl. Instrum. Meth. A **1049**, 168086 (2023). https://doi.org/10.1016/j.nima.2023.168084
4. M. Hartmann, D. Kiselev, D. Reggiani et al., Design of the 590 MeV proton beamline for the proposed TATTOOS isotope production target at PSI. J. Phys: Conf. Ser. **2420**, 012105 (2023). https://doi.org/10.1088/1742-6596/2420/1/012105
5. J.K. Boahen, A.S.G. Khalil, M.A. Hassan et al., EJUSTCO: Monte Carlo radiation transport code hybrid with ANN model for gamma-ray shielding simulation. Nucl. Sci. Tech. **34**, 144 (2023). https://doi.org/10.1007/s41365-023-01297-x
6. Z. Duan, J.H. Chen, H. Shi et al., Using a pre-kicker to ensure safe extractions from the HEPS storage ring. Nucl. Sci. Tech. **32**, 136 (2021). https://doi.org/10.1007/s41365-021-00974-z
7. C.C. Xiao, J.Q. Zhang, J.H. Tan et al., Design and preliminary test of the LLRF in C band high-gradient test facility for SXFEL. Nucl. Sci. Tech. **31**, 100 (2020). https://doi.org/10.1007/s41365-020-00806-6
8. C. Yuan, W. Zhang, T. Ma et al., Design and implementation of accelerator control monitoring system. Nucl. Sci. Tech. **34**, 56 (2023). https://doi.org/10.1007/s41365-023-01209-z
9. H. Liu, G.H. Lei, H.F. Huang, Review on synergistic damage effect of irradiation and corrosion on reactor structural alloys. Nucl. Sci. Tech. **35**, 57 (2024). https://doi.org/10.1007/s41365-024-01415-3
10. B. Goddard, V. Kain, V. Mertens et al., TT40 Damage during 2004 High Intensity SPS Extraction. CERN AB-Note-2005-014 BT (2005)
11. A. Drees, O. Biletskyi, D. Bruno et al., RHIC Quench Protection Diode Radiation Damage. Paper presented at Proceeding of North American Particle Accelerator Confernce (NAPAC'19), pp. 831–833
12. J. Zhang, Y.Q. Wang, J.A. Valdez et al., Ion irradiation-induced phase transformations in phases of Sc2O3–ZrO2 mixtures. Nucl. Instrum. Meth. B **272**, 244 (2012). https://doi.org/10.1016/j.nimb.2011.01.075
13. M.H. Cui, T.L. Shen, H.P. Zhu et al., Vacancy like defects and hardening of tungsten under irradiation with He ions at 800°C. Fusion Eng. Des. **121**, 313 (2017). https://doi.org/10.1016/j.fusengdes.2017.05.043
14. A. Bertarelli, Beam-induced damage mechanisms and their calculation. Paper presented at Proceedings of the 2014 Joint International Accelerator School on Beam Loss and Accelerator Protection, Newport Beach, United States, 2014, edited by R. Schmidt (CERN, Geneva, 2016), pp. 159–227
15. H.J. Wang, Y. Yuan, J.Y. Tang et al., Design of the upstream decay pipe window of the long baseline neutrino facility. Nucl. Sci. Tech. **32**, 129 (2021). https://doi.org/10.1007/s41365-021-00960-5
16. H.T. Wang, H.Q. Jiang, R.F. Shen et al., Electron-beam radiation effects on the structure and properties of polypropylene at low dose rates. Nucl. Sci. Tech. **29**, 87 (2018). https://doi.org/10.1007/s41365-018-0424-y
17. X. Du, T.T. Wang, B.H. Duan et al., Effects of energy deposition on mechanical properties of sodium borosilicate glass irradiated by three heavy ions: P, Kr, and Xe. Nucl. Sci. Tech. **30**, 115 (2019). https://doi.org/10.1007/s41365-019-0632-0
18. L.Q. Zhang, C.H. Zhang, C.C. Hao et al., Mechanical properties and surface characteristics of SiC fibers irradiated by swift heavy ions. Nucl. Sci. Tech. **33**, 113 (2022). https://doi.org/10.1007/s41365-022-01095-x
19. S. Makarov, S. Dyachkov, T. Pikuz et al., Direct imaging of shock wave splitting in diamond at Mbar pressure. Matter Radiat. Extremes **8**, 066601 (2023). https://doi.org/10.1063/5.0156681
20. S.J. Tan, Y.B. Zhong, H. Cheng et al., Experimental investigation on the characteristics of molten lead–bismuth non-eutectic alloy fragmentation in water. Nucl. Sci. Tech. **33**, 115 (2022). https://doi.org/10.1007/s41365-022-01097-9
21. C. Liu, X.G. Deng, Y.G. Ma, Density fluctuations in intermediate-energy heavy-ion collisions. Nucl. Sci. Tech. **33**, 52 (2022). https://doi.org/10.1007/s41365-022-01040-y
22. R. Li, J.L. Jiao, H. Luo et al., Two-dimensional particle-in-cell modeling of blow-off impulse by X-ray irradiation. Nucl. Sci. Tech. **35**, 53 (2024). https://doi.org/10.1007/s41365-024-01412-6
23. H. Xu, X.H. Yang, Z.M. Sheng et al., Collimation of high-current fast electrons in dense plasmas with a tightly focused precursor intense laser pulse. Nucl. Fusion **59**, 126024 (2019). https://doi.org/10.1088/1741-4326/ab45a2

24. J. Huang, T. Zhang, J. Zhang et al., Observation of local density increase during pellet homogenization on EAST. Nucl. Fusion **64**, 016031 (2024). https://doi.org/10.1088/1741-4326/ad0efa
25. N.A. Tahir, V. Kain, R. Schmidt et al., The CERN large hadron collider as a tool to study high-energy density matter. Phys. Rev. Lett. **94**, 135004 (2005). https://doi.org/10.1103/PhysRevLett.94.135004
26. N.A. Tahir, F. Burkart, R. Schmidt et al., Beam induced hydrodynamic tunneling in the future circular collider components. Phys. Rev. Accel. Beams **19**, 081002 (2016). https://doi.org/10.1103/PhysRevAccelBeams.19.081002
27. D. Walz, D. Busick, T. Constant et al., Tests and description of beam containment devices and instrumentation - a new dimension in safety problems. IEEE Trans. Nucl. Sci. **20**, 465 (1973). https://doi.org/10.1109/TNS.1973.4327151
28. I. Efthymiopoulos, C. Hessler, H. Gaillard et al., HiRadMat: a new irradiation facility for material testing at CERN. Paper presented at 2nd International Particle Accelerator Conference, San Sebastian, Spain, 4–9 Sep 2011, pp. 1665–1667
29. R. Schmidt, J.B. Sancho, F. Burkart et al., First experimental evidence of hydrodynamic tunneling of ultra-relativistic protons in extended solid copper target at the CERN HiRadMat facility. Phys. Plasmas **21**, 080701 (2014). https://doi.org/10.1063/1.4892960
30. F. Burkart, R. Schmidt, V. Raginel et al., Analysis of 440 GeV proton beam–matter interaction experiments at the High Radiation Materials test facility at CERN. J. Appl. Phys. **118**, 055902 (2015). https://doi.org/10.1063/1.4927721
31. L.Q. Qi, G. Li, Y.P. Xu et al., Geant4 simulation for the responses to X-rays and charged particles through the eXTP focusing mirrors. Nucl. Instrum. Meth. A **963**, 163702 (2020). https://doi.org/10.1016/j.nima.2020.163702
32. H. Li, J.L. Chen, J.G. Li et al., High heat load tests on W/Cu mock-ups and evaluation of their application to EAST device. Fusion Eng. Des. **84**, 1–4 (2009). https://doi.org/10.1016/j.fusengdes.2007.12.013
33. T. Yang, J. Tian, L. Zeng et al., Experimental studies and Monte Carlo simulations for beam loss monitors. Phys. Rev. Accel. Beams **24**, 032804 (2021). https://doi.org/10.1103/PhysRevAccelBeams.24.032804
34. Y. Xu, G. Wang, Z. Li et al., Design of beam dump for the commissioning at SHINE facility. Radiat. Prot. 40, 510 (2020) (in Chinese). https://qikan.cqvip.com/Qikan/Article/Detail?id=7103802243
35. G. Battistoni, T. Boehlen, F. Cerutti et al., Overview of the FLUKA code. Ann. Nucl. Energy **82**, 10–18 (2015). https://doi.org/10.1016/j.anucene.2014.11.007
36. S. Mallows, I. Azhgirey, I. Bayshev et al., Monte Carlo simulations of the radiation environment for the CMS experiment. Nucl. Instrum. Meth. A **824**, 30 (2016). https://doi.org/10.1016/j.nima.2015.11.044
37. S. Agostinelli, J. Allison, K. Amako et al., Geant4–a simulation toolkit. Nucl. Instrum. Meth. A **506**, 250 (2003). https://doi.org/10.1016/S0168-9002(03)01368-8
38. C.C. Wang, J.N. Hu, Y. Zhang et al., Properties of nuclear matter in relativistic Brueckner–Hartree–Fock model with high-precision charge-dependent potentials. J. Phys. G: Nucl. Partic. **47**, 105108 (2020). https://doi.org/10.1088/1361-6471/aba423
39. A. Capriccioli, P. Frosi, Multipurpose ANSYS FE procedure for welding processes simulation. Fusion Eng. Des. **84**, 546 (2009). https://doi.org/10.1016/j.fusengdes.2009.01.039
40. Y.C. Ma, X.L. Zhao, X.H. Ye et al., A transient fluid–structure interaction analysis strategy and validation of a pressurized reactor with regard to loss-of-coolant accidents. Nucl. Sci. Tech. **31**, 54 (2020). https://doi.org/10.1007/s41365-020-00771-0
41. Y.H. Zhang, Nonrecursive residual Monte Carlo method for SN transport discretization error estimation. Nucl. Sci. Tech. **33**, 61 (2022). https://doi.org/10.1007/s41365-022-01042-w
42. D.H. ShangGuan, W.H. Yan, J.X. Wei et al., Sample size adaptive strategy for time-dependent Monte Carlo particle transport simulation. Nucl. Sci. Tech. **34**, 58 (2023). https://doi.org/10.1007/s41365-023-01202-6
43. E. Quaranta, A. Bertarelli, R. Bruce et al., Modeling of beam-induced damage of the LHC tertiary collimators. Phys. Rev. Accel. Beams **20**, 091002 (2017). https://doi.org/10.1103/PhysRevAccelBeams.20.091002
44. N.A. Tahir, F. Burkart, R. Schmidt et al., Review of hydrodynamic tunneling issues in high power particle accelerators. Nucl. Instrum. Meth. B **427**, 70 (2018). https://doi.org/10.1016/j.nimb.2018.04.009
45. N.A. Tahir, F. Burkart, A. Shutov et al., Simulations of beam-matter interaction experiments at the CERN HiRadMat facility and prospects of high-energy-density physics research. Phys. Rev. E **90**, 063112 (2014). https://doi.org/10.1103/PhysRevE.90.063112
46. V.E. Fortov, B. Goel, C.-D. Munz et al., Numerical simulations of nonstationary fronts and interfaces by the Godunov Method in Moving Grids. Nucl. Sci. Eng. **123**, 169 (1996). https://doi.org/10.13182/NSE96-A24181
47. Y. Nie, C. Fichera, L. Mettler et al., Simulation of hydrodynamic tunneling induced by high-energy proton beam in copper by coupling computer codes. Phys. Rev. Accel. Beams **22**, 014501 (2019). https://doi.org/10.1103/PhysRevAccelBeams.22.014501
48. L. Burakovsky, D.L. Preston, S.D. Ramsey et al., Shock standards Cu, Ag, Ir, and Pt in a wide pressure range. Matter Radiat. Extremes **8**, 046901 (2023). https://doi.org/10.1063/5.0124555
49. G.R. Johnson, A constitutive model and data for metals subjected to large strains, high strain rates and high temperatures. Paper presented at Proceedings of the 7th International Symposium on Ballistics, The Hague, Netherlands (1983)
50. G.R. Johnson, W.H. Cook, Fracture characteristics of three metals subjected to various strains, strain rates, temperatures and pressures. Eng. Fract. Mech. **21**, 31 (1985). https://doi.org/10.1016/0013-7944(85)90052-9